Nano Energy 76 (2020) 105037

Contents lists available at ScienceDirect

Nano Energy

journal homepage: http://www.elsevier.com/locate/nanoen

Ultrahigh field-induced strain in lead-free ceramics

Jiyue Wu [a,b], Haibin Zhang [c], Chang-Hsun Huang [d], Chiao-Wei Tseng [b], Nan Meng [a], Vladimir Koval [e], Yi-Chia Chou [d], Zhen Zhang [b,*], Haixue Yan [a,f,**]

[a] School of Engineering and Materials Science, Queen Mary University of London, Mile End Road, London, E1 4NS, UK
[b] Division of Solid-State Electronics, Department of Electrical Engineering, Uppsala University, Lagerhyddsvagen, Uppsala, Sweden
[c] Innovation Research Team for Advanced Ceramics, Institute of Nuclear Physics and Chemistry, China Academy of Engineering Physics, Mianyang, 621900, China
[d] Department of Electrophysics, National Chiao-Tung University, Hsinchu, 30010, Taiwan
[e] Institute of Materials Research, Slovak Academy of Sciences, Watsonova 47, 04001, Kosice, Slovakia
[f] NPU-QMUL Joint Research Institute of Advanced Materials and Structure, Northwestern Polytechnical University, Xi'an, 710072, PR China

ARTICLE INFO

Keywords:
Lead-free ceramics
Piezoelectric
Strain
Phase transitions
Polar nanoregions

ABSTRACT

Due to the worldwide concerns of environmental protection and sustainable development, lead-free piezoelectric materials are greatly desired for bridging the electrical energy to the mechanical energy. However, their lower energy conversion coefficient compared to the conventional lead-containing piezoelectric materials significantly limits their device applications. Herein, we introduce a novel strategy to increase the strain of lead-free ferroelectric system via material structure design to create polar nano regions (PNRs) and point defects in the material while retaining the global ferroelectric phase. This added short-range structural heterogeneity in the material will facilitate the field-induced phase transition and reversible domain wall switching to enhance the strain. Following this strategy, we demonstrate an ultrahigh strain induced by an electric field in non-textured lead-free $Bi_{0.5}Na_{0.5}TiO_3$ (BNT)-based ceramics. The strain in unipolar mode (S_{uni}) can reach up to 0.74% at 70 kV/cm, making it the highest value in reported lead-free ceramics so far. This puts forward a good route to design high-performance piezoelectric materials by material structure engineering. It also reveals the promising potential of lead-free piezoelectric materials in practical electromechanical device applications.

1. Introduction

With the valuable capability to convert between electrical energy and mechanical energy, piezoelectric materials have numerous important electromechanical device applications in the modern society today, such as actuators, transducers, sensors and ultrasonic motors [1–4]. Currently, lead-based ceramics (such as Pb(Zr, Ti)O_3 (PZT) and Pb$(Mg_{1/3}Nb_{2/3})O_3$–$PbTiO_3$ (PMN-PT)) are the most widely-chosen materials for manufacturing commercial electromechanical devices [5,6], owing to their unparalleled electromechanical properties at the morphotropic phase boundary (MPB) [7]. However, due to the global concern of environment-friendly development of human society, lead is legislated to be eliminated for practical use because of the toxicity of lead evaporation during the material sintering process. Thus, achieving high-performance lead-free piezoelectric systems have been the key direction of the research on piezoelectric ceramics [8,9].

Comparing to the commercialized lead containing materials, lead-free piezoelectric materials exhibit lower output of mechanical energy converted from electrical energy, in terms of lower field-induced strain values [10]. Meanwhile, they require large poling field and possess slow kinetics of domain switching (response speed) as well [11]. These challenges greatly hinder the practical device applications of lead-free piezoelectric materials. The origin of the field-induced strain can be divided into intrinsic and extrinsic contributions: intrinsic contributions include electrostriction, piezoelectric effect and volume change of unit cell induced by phase transitions, while extrinsic contributions involve ferroelectric domain switching and point defects. Normally, the main contributions to the field-induced strain in ferroelectrics are field-induced phase transitions, domain switching and point defects [12–15]. Here, we aim to enhance these three main contributions by compositional-driven material nanostructure design to enlarge the field-induced strain value in a lead-free polycrystalline ceramic system.

As a promising lead-free alternative in the piezoelectric family, bismuth sodium titanate ($Bi_{0.5}Na_{0.5}TiO_3$, BNT) is selected in this study

* Corresponding author. Division of Solid-State Electronics, Department of Electrical Engineering, Uppsala University, Lagerhyddsvagen, Uppsala, Sweden.
** Corresponding author. School of Engineering and Materials Science, Queen Mary University of London, Mile End Road, London, E1 4NS, UK.
E-mail addresses: zhen.zhang@angstrom.uu.se (Z. Zhang), h.x.yan@qmul.ac.uk (H. Yan).

https://doi.org/10.1016/j.nanoen.2020.105037
Received 2 May 2020; Received in revised form 29 May 2020; Accepted 29 May 2020
Available online 18 June 2020

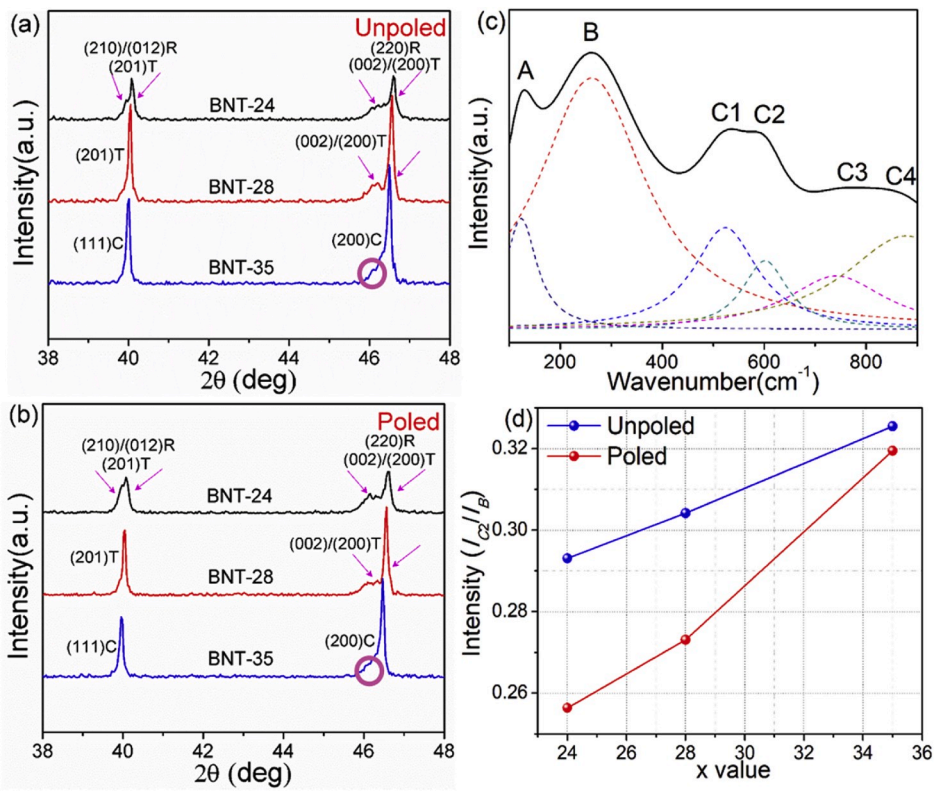

Fig. 1. XRD patterns of the (a) unpoled and (b) poled (5 kV/mm for 15 min) samples of BNT-X ceramics (X = 24, 28 and 35) within the 2θ range from 38° to 48°. The two characteristic reflections are distinguished in both samples, respectively. R, T and C represents the rhombohedral, tetragonal and cubic phase, respectively. The split and the 'shoulder' of the reflections are marked with pink arrows and circles, respectively. (c) Six peaks are deconvoluted from the Raman spectra based on the Lorentzian functions, taking unpoled BNT-24 as an example. (d) The intensity ratio of *C*2 and *B* Raman modes before and after poling (I_{C2}/I_B) as a function of x value.

owing to their structural flexibility as well as their field-induced transition behaviour [16]. Enormous attention has been attracted to optimizing strain values in BNT-based ceramics since a breakthrough was achieved in BNT-BT-KNN ($Bi_{0.5}Na_{0.5}TiO_3$–$BaTiO_3$–$K_{0.5}Na_{0.5}NbO_3$) system by Zhang et al. [17] The unipolar strain was reported to be 0.45% at 80 kV/cm with a corresponding d_{33}* of 560 pm/V due to the field-induced antiferroelectric-ferroelectric phase transitions, exceeding the values of some PZT-based materials and other lead-free systems. Later on, according to the latest findings by Tan et al., another significantly improved strain (~0.70%) was achieved in non-textured $Bi_{0.5}Na_{0.5}TiO_3$ (BNT)-based ceramics due to the reversible field-induced phase transitions between ergodic relaxor phases (space group *R*3*c* and *P*4*bm*) and ferroelectric phase (space group *R*3*c*). [12] In piezoelectrics, the highest strain induced by an electric field was observed in $Pb(Mg_{1/3}Nb_{2/3})O_3$–$PbTiO_3$ (PMN-PT) materials, which was attributed to the local structural engineering based on polar nano regions (PNRs) in the Pb-based ferroelectrics [18]. Despite the intensive study on the field-induced phase transitions, the other two main contributions such as domain wall switching and point defects can also be vital to enhance strain values in BNT-based materials.

In this work, we aim at raising the field-induced strain values in the BNT-based ceramics by enhancing all the three main contributions to the strain output. Our strategy is to engineer the material structure to create more PNRs while retaining the global ferroelectric phase to facilitate field-induced phase transitions. In addition, point defects will be introduced to improve the reversibility of domain switching. In detail, the structural engineering of BNT was realized by the chemical modification: Sr^{2+} was introduced at A-site to weaken the ferroelectricity and disrupt the long-range ferroelectric order of BNT to create PNRs, which can enhance the field-induced phase transitions [19]. Another co-doping element, Li^+ can increase the structural inhomogeneity and create PNRs. In addition, Li^+ doping also results in a more flexible lattice due to its comparatively small ionic radius (0.092 nm for Li^+, 0.117 nm for Bi^{3+} and 0.136 nm for Na^+), making the system more sensitive to the electric field [20]. We expect that the strain value can be further increased by the Li^+ doping due to the elevated electric field sensitivity. With these considerations, we prepared the solid solutions of $Sr_x(Bi_{1-x}Na_{0.97-x}Li_{0.03})_{0.5}TiO_3$ (x = 0.24, 0.28 and 0.35, abbreviated afterwards as BNT-24, BNT-28 and BNT-35) via the conventional solid-state fabrication route. High sintering temperature (above 1130 °C) [21] were used to create oxygen vacancies.

2. Experiment and methods

2.1. Material preparation

The ceramic samples of $Sr_x(Bi_{1-x}Na_{0.97-x}Li_{0.03})_{0.5}TiO_3$ (x = 0.24, 0.28 and 0.35, named as BNT-24, 28 and 35) were fabricated via a solid-state reaction method. Powders of Bi_2O_3 (99.9% Sigma-Aldrich), Na_2CO_3 (99.5% Sigma-Aldrich), TiO_2 (99.8% Sigma-Aldrich), $SrCO_3$ (99.5% Alfa Aesar), and Li_2CO_3 (99.0% Alfa Aesar) were selected as raw materials. All the precursors were preheated at 200 °C overnight before weighing according to the stoichiometry. Then, the powders were mixed thoroughly and ball-milled in ethanol for 4 h. After drying at 100 °C overnight in air, the mixture was calcined at 800 °C for 2 h followed by 900 °C for 4 h. A second round of ball-milling was conducted for another 4 h to obtain the homogenous particle size. The dried powders were cold pressed into pellets under a uniaxial pressure of 70 MPa. The pellets were sintered at 1100 °C and 1150 °C for 4 h for densification, respectively. The sintering was carried out in buried calcined powders to avoid the evaporation of Bi, Na and Li.

2.2. Characterization

The density of all pellets for characterization was guaranteed over 95% of theoretical density. The microstructure was examined on the fracture surface using a FEI Inspect F (Hillsboro, OR) scanning electron microscope (SEM). The phase structure was characterized using X-ray diffraction (XRD) on crushed pellets, using a PANalytical X'Pert Pro X-ray diffractometer (PANalytical, Cambridge, UK). It was fitted with a

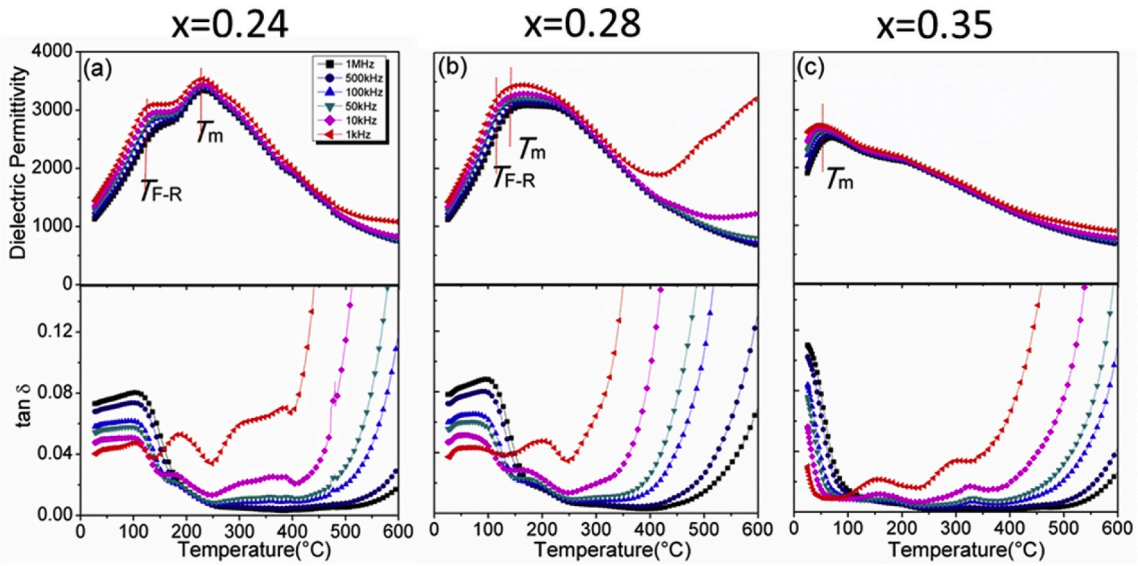

Fig. 2. Temperature dependence of dielectric permittivity and loss for BNT-X ceramics at six different frequencies from 25 °C to 600 °C: (a) X = 24, (b) X = 28 and (c) X = 35.

X'Celerator detector in θ/θ geometry using Ni filtered Cu-Kα radiation (λ = 1.5418 Å). XRD results were analysed by the Rietveld method using the FullProf program The Piezoresponse Force Microscopy (PFM) (NT-MDT, Ntegra systems, Russia) was employed to examine the local domain structure, using a conductive tip operated at 50 kHz with a AC electric field. The AFM probe (HQ:NSC18/Pt, MikroMasch) is equipped with a conductive tip (radius of about 30 nm, Pt coating). Raman spectroscopy was performed by a Confocal Raman Microscope (Model InVia, Renishaw, New Mills, UK) with a laser wavelength of 532 nm, 1 mW of laser power and an objective of 50 × in the backscattering configuration. A transmission electron microscope (TEM) (JEOL ARM200F) operated at 200 kV was employed for TEM observation. The TEM specimen was prepared using dual-beam focus ion beam microscope (TESCAN LYRA3) with 30 kV Ga ion beam. For SHG measurements, two laser beams from a femtosecond optical parametric oscillator (Insight DS+, Newport, CA) were used as the light source for the microscope. The tuneable oscillator output in the wavelength range between 800 nm and 1100 nm was used to excite the samples. The emission photons were collected through the same microscope objective, then optically filtered and detected with a photomultiplier tube.

Prior to electrical characterization, all the pellets were grinded and polished with SiC sandpaper to obtain a smooth surface. Silver paste (Gwent Electronic Materials Ltd., C2011004D5, Pontypool, U.K.) was homogenously covered on the top and bottom of discs with an average thickness of around 0.3 mm, and then fired at 600 °C for 30 min to obtain smooth electrodes for electrical characterization. The temperature dependence of dielectric constant (ε_r) and loss (tan δ) was measured at six different frequencies in the range of 1 kHz to 1 MHz using an LCR meter (Agilent, 4284A, Hyogo, Japan) with controlled temperature from room temperature to 600 °C. The Current Density-Electric field (*J-E*), Electric Displacement-Electric field (*D-E*) and Strain-Electric field (*S-E*) hysteresis loops were measured at the frequency of 1 Hz using a hysteresis tester (NPL, Teddington, U.K.) and triangle waveforms. A special probe for the simultaneous measurement of electrical current and mechanical displacement was built (collaborated with NPL, Teddington, U.K), consisting of a pair of NXB2-AL nano-sensors, which convert the mechanical displacement into a voltage, with the sensitivity in the order of nanometres. The sensor is driven by a single channel NS2000 controller. The output from the NS2000 is sent to a digital voltmeter for data acquisition. All the data in the ferroelectric tests are repeatable as they were obtained in ten samples for each composition. The samples were poled at a DC field of 5 kV/mm for 15 min at room temperature. The d_{33} values were examined using a quasi-static ZJ-3B PIEZO meter (Institute of Acoustics Academia Sinica, China).

3. Results and discussion

3.1. Global and local structure

Fig. 1 shows the room-temperature XRD patterns of BNT-x ceramics before and after poling. In Fig. S1(a), the XRD reflections can be indexed to a perovskite structure with different phases for each composition. Within the magnification of 2θ range between 38° and 48° (Fig. 1(a)), the split of both (210)/(012)R and (002)/(200)T reflections can be detected in BNT-24, suggesting the coexistence of rhombohedral (R) and tetragonal (T) phases [22]. In BNT-28, a single (201)T reflection and the split of the (002)/(200)T reflection is detected, which indicates the tetragonal phase. In BNT-35, the pseudo-cubic (C) phase is identified as the 'shoulder' at the (200)C reflection suggests the tetragonal distortion. To sum up, the overall structure becomes less distorted with the increase of Sr in the system. For comparison, the XRD patterns of the BNT-x ceramics after poling (poling at 5 kV/mm for 15 min) were examined as well (shown in Fig. S1(b)). In order to clarify the structural changes after poling, the deconvolution of the XRD patterns was performed considering the Gaussian function as the shape of the resolved peaks. For BNT-24, the values of 2θ corresponding to the centre position of the four reflections are determined based on the deconvolution results of the corresponding XRD patterns before and after poling, respectively (shown in Figs. S1(c) and S1(d)). The 2θ values of the centre position corresponding to (002)T and (200)T reflection is 46.25° and 46.60°, respectively. After poling, the 2θ value of the (002)T reflection shifts to a slightly smaller angle (46.18°) while that of the (200)T stays unchanged, which indicates the increase of the lattice distortion after poling. Comparatively, for BNT-28 and BNT-35, no change is detected after poling according to their signature reflections. Hence, the irreversible field-induced phase transitions are proved in BNT-24.

With the global crystal structure defined by XRD patterns, Raman spectroscopy was employed to reveal the details of local lattice dynamics in BNT-x ceramics [23]. As shown in Fig. S2(a) (b), all the Raman modes of unpoled and poled samples exhibit a diffused and broadened style, which can be attributed to the disorder of cations in A-site or distorted octahedral clusters [24]. In addition, the intense broad bands result from the overlapping of the Raman modes, suggesting the characteristic relaxor behaviour [25]. The Raman spectra were deconvoluted

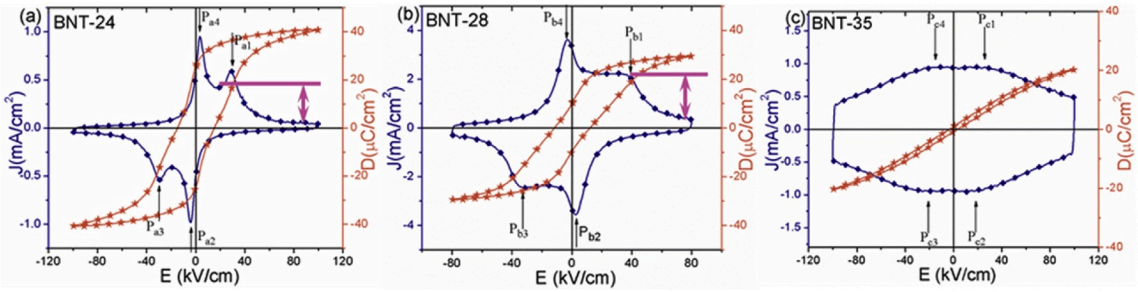

Fig. 3. Current density-electric field (*J-E*) and electrical displacement-electric field (*D-E*) loops of (a) BNT-24, (b) BNT-28, and (c) BNT-35 ceramics. All samples were tested at different electric field amplitudes and 10 Hz frequency. The pink arrows show the decrease in current density which is related to field induced transition.

into six peaks [23] based on the Gaussian-Lorentzian function (The fitting result of unpoled BNT-24 is given as an example in Fig. 1(c)). All the Raman modes can be divided into three regions: region A (mode *A*, the wavenumber below 200 cm^{-1}) is associated with the vibration of A-site cations; region B (mode *B*, the wavenumber between 200 and 450 cm^{-1}) is related to the vibration of Ti–O bond and region C (mode *C*1, *C*2, *C*3 and *C*4, wavenumber above 450 cm^{-1}) is consistent with [TiO_6] octahedral vibrations, the so-called breathing and stretching modes [23]. It can be distinguished that the *C*2 mode shifts to the higher wavenumber (weak blueshift) after poling marked in Fig. S2(a) (b) due to the field-induced strengthened polar state. For BNT-based materials, the local field-induced phase transitions from non-polar state to ferroelectric state are supported by the reduction in the intensity ratio of *C*2 and *B* modes [26]. As shown in Fig. 1(d), the intensity ratio of *C*2 and *B* modes (I_{C2}/I_B) are plotted as a function of x value. The ratio experiences a significant decrease after poling for BNT-24 and BNT-28, indicating that the local structure transforms into a stronger polar state [23]. Comparatively, the drop of I_{C2}/I_B for BNT-35 after poling is less prominent, suggesting the lack of long-range ferroelectric order after poling in BNT-35. It should be noted that the Raman results also evidence the existence of local structure distortion in BNT-35, which is identified as cubic structure based on the XRD results.

3.2. Temperature-dependent dielectric properties

Fig. 2 shows the temperature dependence of dielectric permittivity (ε_r) and loss tangent (tan δ) for unpoled BNT-x samples. Six different frequencies were selected in the range from 1 kHz to 1 MHz in the temperature range from 25 °C to 600 °C. Strong frequency dispersion of ε_r and tan δ is observed for all the three materials, which is a fingerprint of relaxor ferroelectrics. In the ε_r - *T* spectrum, the BNT-based systems typically exhibit two dielectric anomalies: named as $T_{F\text{-}R}$ (the temperature corresponding to the 'shoulder' in the dielectric spectrum) and T_m (the temperature corresponding to the peak in the dielectric spectrum). $T_{F\text{-}R}$ is the ferroelectric-to-relaxor transition temperature, above which macroscale ferroelectric domains are unstable and only PNRs exist [27]. Generally speaking, $T_{F\text{-}R}$ should be above room temperature for BNT-based materials to possess excellent piezoelectric properties contributed from both ferroelectric domains and PNRs; T_m can be explained as result of a change in size and dynamics of polar regions, rather than related to any phase transition behaviour [28].

As shown in Fig. 2(a), the ε_r - *T* spectrum of BNT-24 exhibits two anomalies. The first anomaly $T_{F\text{-}R}$ (~127 °C) shifts to a higher temperature with the increase of frequency. Correspondingly, the anomaly appears at the same position in the tan δ - *T* spectrum. T_m occurs at ~230 °C for BNT-24, above which ε_r starts to decrease monotonically. As the ferroelectric-to-relaxor transition temperature $T_{F\text{-}R}$ (above which the piezoelectric properties degrade) can be regarded as the maximum working temperature for actuator applications [29], the limited working temperature of our BNT-24 ceramics is about 127 °C. In Fig. 2(b), the $T_{F\text{-}R}$ of BNT-28 shifts to a lower temperature (~122 °C). The peak of BNT-28 at T_m (~158 °C) is more flattened compared with BNT-24. For BNT-35, there is only one anomaly peak T_m (~52 °C) in the ε_r - *T* spectrum (Fig. 2(c)) and the corresponding ε_r value is the lowest. With the increasing content of Sr, T_m shifts to a lower value, suggesting the weakening of the polar structure. In the tan δ - *T* spectrum, the presence of the dielectric loss peaks may indicate different underlying mechanisms: the first loss anomaly (below $T_{F\text{-}R}$) is contributed from ferroelectric domains together with PNRs, while the latter two loss anomalies (above $T_{F\text{-}R}$) are contributed from PNRs and oxygen vacancies [30]. The dielectric analysis is consistent with the XRD and Raman results.

3.3. Ferroelectric properties

Current density-electric field (*J-E*) and electric displacement-electric field (*D-E*) loops of all samples are shown in Fig. 3. Four current peaks can be seen in all *J-E* loops, but the shapes and positions vary. Based on the discussion above, the mechanism of the current peaks for BNT-24 can be interpreted as the combination of domain switching and field-induced phase transitions [31]. As shown in Fig. 3(a), the current density in the first quadrant decreases (marked using a pink arrow) when the applied field is above the position of P_{a1} peak during the loading of a positive field, which is related to field-induced transitions from a weak polar state, dominated by PNRs, to a strong polar state. The field-induced phase transitions are irreversible in BNT-24, which is supported by that there is no current density peak in the fourth quadrant during the unloading of the field. When a negative field is applied, the strong polar state turns into a weak polar state when the applied field is above the position of P_{a2} peak, which is also related to the increased current density in the third quadrant due to the contribution of PNRs in the weak polar state. The strong polar state is also stable during the unloading of the negative field, which is consistent with that there is no current peak in the second quadrant. The strong polar state turns into a weak polar state including PNRs when the applied positive field is above the position of P_{a4} peak. Moreover, the current density peaks P_{a1} in the first quadrant and P_{a3} in the third quadrant can be attributed to the ferroelectric domain switching under the applied field [32–34]. For BNT-28, as shown in Fig. 3(b), the first broad peak (P_{b1}) indicates the weak domain switching behaviour plus the field-induced phase transitions, which is related to the decrease of current density in the first quadrant. Different from BNT-24, the second peak (P_{b2}) in the fourth quadrant, which is related to the transition from the strong polar phase to weak polar state, occurs before the positive field returns to zero, suggesting that the field-induced transitions in BNT-28 are reversible. Similarly, the peaks (P_{b3} and P_{b4}) share the same story during the loading and unloading of the negative electric field. Compared with the original polar state of BNT-28, the polar state of BNT-28 was strengthened after the positive field was unloaded, in terms of the distinct remnant electrical displacement (D_r, *D* value at zero field). Therefore, the field-induced phase transitions are not fully reversible in BNT-28. For BNT-35 (Fig. 3(c)), the first broad peak (P_{c1}) indicates that the PNRs transform to a strong polar state and the second peak P_{c2} indicates

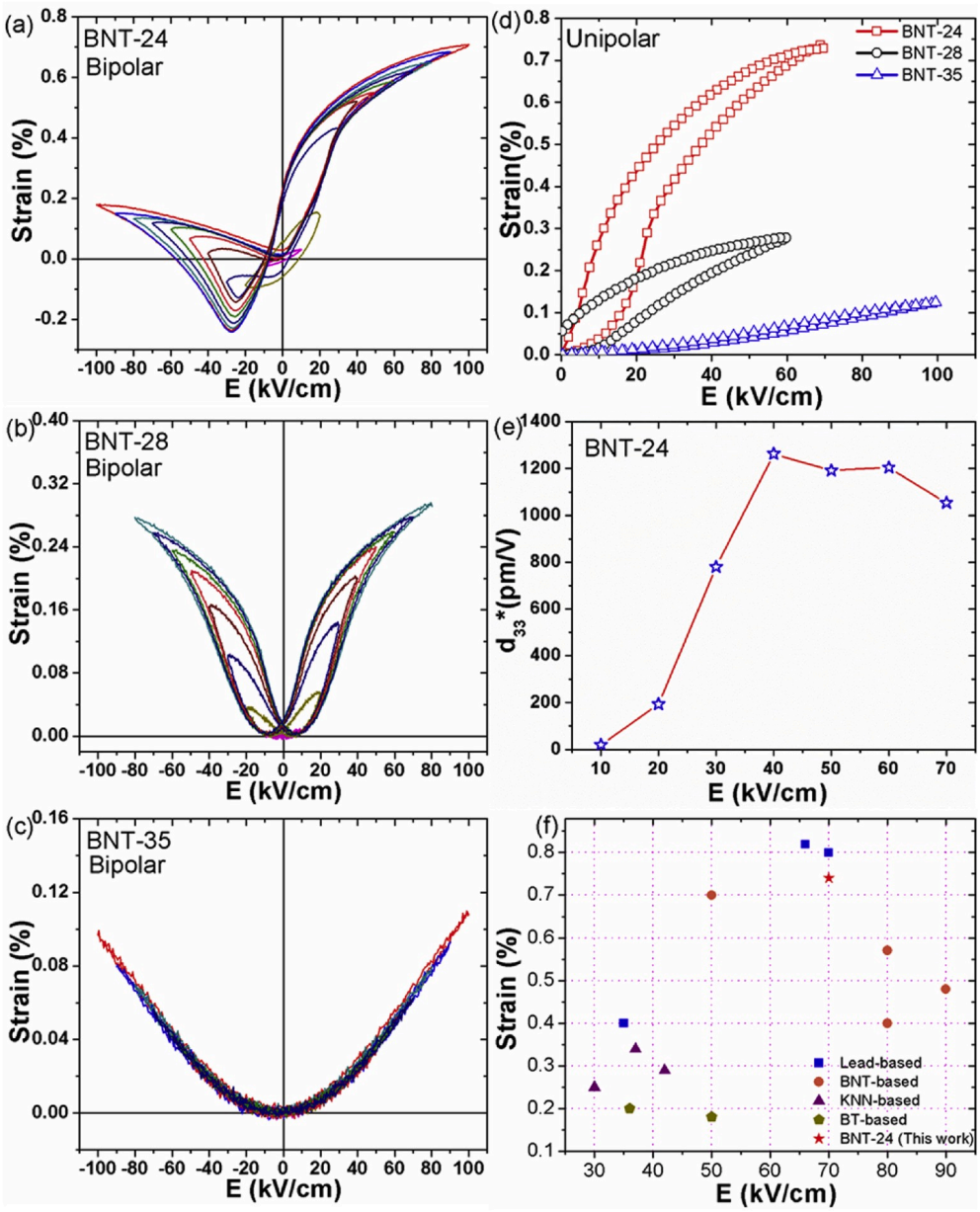

Fig. 4. Bipolar strain-electric field (*S-E*) loops of (a)BNT-24, (b)BNT-28, and (c) BNT-35 ceramics. All samples were tested at different electric field amplitudes and 1 Hz frequency. (d) Unipolar strain-electric field (*S-E*) loops of BNT-x samples. (e) d_{33}* values as a function of electric field of BNT-24. (f) Comparison of strain values in representative lead-free and lead-containing ceramics [12,42–52].

that the strong polar state goes back to relaxor state. The current value stays the same as the original value after the positive field is unloaded, which shows that there is no irreversible part in the field-induced phase transitions in BNT-35. In addition, there is no evidence of domain switching with the applied field for BNT-35, confirming its ergodic relaxor state. Correspondingly, the *D-E* loops get more pinched with the increasing content of Sr^{2+}, indicating the weakening of the original polar state. For BNT-24 and BNT-28 (Fig. 3(a)(b)), the *D-E* loops are ferroelectric-like and show an impressive saturated electrical displacement (D_{sa}), a large D_r and coercive field (E_c). On the contrary, BNT-35 (Fig. 3(c)) exhibits relaxor-like slim *D-E* loops with a moderate D_{sa} and negligible D_r.

In order to investigate the polar state evolution with temperature, ferroelectric properties were characterized with the continuous change of temperature from room temperature to 110 °C, below T_{F-R} (Figs. S3 and S4). Taking BNT-24 as an example, the electric field corresponding to P_{a1} shifts to a higher value while that corresponding to P_{a4} shifts from positive to negative with temperature increasing (marked in Fig. S3(a)). It indicates the increase of thermal instability of the polar state, which agrees well with previous discussion. Meanwhile, the weakening of the original polar state with the increase of temperature can be evidenced by the decrease of the current density values at P_{a1} and P_{a4}, and the *D-E* loops (Fig. S3(a)) are more relaxor-like with the continuous decreasing D_r and D_{sa} (Fig. S3(b)). The same story of thermal degradation of the polar state can be detected in BNT-28 (Fig. S4).

3.4. Electro-strain behavior

Bipolar strain-electric field curves (*S-E*) of all three compositions are shown in Fig. 4(a)-(c). The bipolar *S-E* curves of BNT-24 exhibit a butterfly-like shape with negative strain, which is typical for ferroelectrics including switching of non-180° domain walls. The maximum strain value is obtained from the maximum positive value to the maximum negative value, which is 0.93% for BNT-24 at the electric field

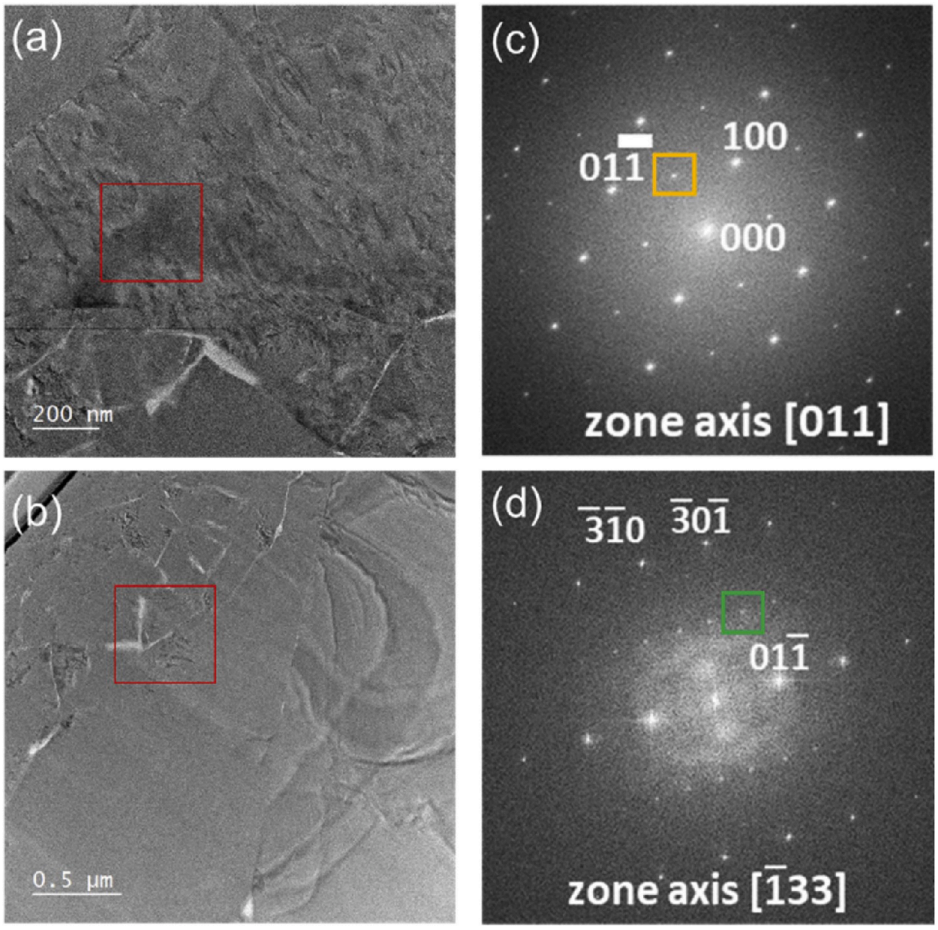

Fig. 5. Bright field TEM images of the selected area inside the grains of BNT-24 ceramics displayed (a) along the [011] zone axis and (b) along the [1 33] zone axis. The Selected Area Electron Diffraction (SAED) patterns were recorded under the (c) [011] zone axis and (d) the [1 33] zone axis from the area marked in red in (a) and (b), respectively. The patterns showing $\frac{1}{2}\{ooo\}$ and $\frac{1}{2}\{ooe\}$ super-lattice reflections are highlighted with orange and green squares, respectively.

of 100 kV/cm. The four current peaks in *J-E* loops in Fig. 3(a) and the *S-E* loops in Fig. 4(a) indicate that the giant strain includes contributions from the field-induced weak polar to strong polar phase transition and the non-180° domain wall switching. This is consistent with the findings of Jo et al. [35] Similar phenomenon was also evidenced by the in-situ TEM [36] and neutron diffraction [37] in $Bi_{0.5}Na_{0.5}TiO_3$–$BaTiO_3$ (BNT-BT). In addition, the asymmetric shape of the *S-E* curves also indicates the existence of a strong internal bias field which is caused by the charged defects (oxygen vacancies) [12,38]. These defects are common in BNT-based ceramics due to high temperature sintering. These defects may provide additional storing force of the recoverable domain switching, which can also enhance the strain values [39]. Indeed, the strain response of the BNT-24 sample sintered at high temperature (1150 °C for 4 h) for oxygen vacancies creation is much larger than that of the BNT-24 sintered at 1100 °C for 4 h (which has a symmetric-shape *S-E* curve as shown in Fig. S5). It should be noted that the asymmetric shape is not so obvious in the corresponding *D-E* loops in Fig. 3(a), which suggests that *S-E* loops are more sensitive to internal bias field induced by point defects [38]. Different from BNT-24, BNT-28 shows symmetric butterfly-like loops with a negligible negative value owing to the weak polar state without non-180° domain walls. Thus, its strain value is reduced (0.28% at 80 kV/cm). At last, the *S-E* loops of BNT-35 are sprout-shaped and feature electrostrictive-like behaviour, matching the paraelectric phase at global scale. It shows the lowest strain value as well (0.10% at 100 kV/cm) contributed only from electrostriction.

In practical piezoelectric applications, the evaluation criterion of strain is mainly based on the unipolar strain value (S_{uni}) and large-signal piezoelectric coefficient (d_{33}*). Herein, *S-E* curves tested with unipolar electric field are shown in Fig. 4(d). For all the three materials, the unipolar strain increases with the increase of the applied electric field. It should be noted that the maximum applied field is 10 kV/cm lower than the breakdown field of the sample. Consistent with the strain performance under bipolar field, BNT-24 possesses the highest S_{uni} value (0.74%) at 70 kV/cm. The corresponding value of d_{33}* is 1057 pm/V. In Fig. 4(e), the giant d_{33}* value (1263 pm/V) was triggered at a low electric field (40 kV/cm), showing tremendous potential in application of electromechanical devices such as sensors and actuators. The S_{uni} of BNT-24 is the highest among the lead-free ceramics reported so far and is very close to the value (~0.8%) of lead-based ceramics as well, which is shown in Fig. 4(f). Hence, BNT-24 has been shown to have great potential to take over the electromechanical devices market in the future, with their strain values close to those of lead-based ceramics.

3.5. On the origin of the giant electro-strain

To further verify the contribution of the giant strain of BNT-24 at microscale, piezoresponse force microscopy (PFM) was carried out on BNT-24. The out-of-plane PFM phase images on the 5*5 μm^2 area of the polished and thermal-etched surface were captured before and after poling (Fig. S6). No clear domain walls were observed in Fig. S6(a), which suggests that the most of domain size is too small to meet the limitation scale of the PFM (~10–25 nm) [40]. After poling with a DC bias voltage on the 3*3 μm^2 area (+50 V on the top half and - 50 V on the bottom half), the strengthened polar state can be confirmed by the

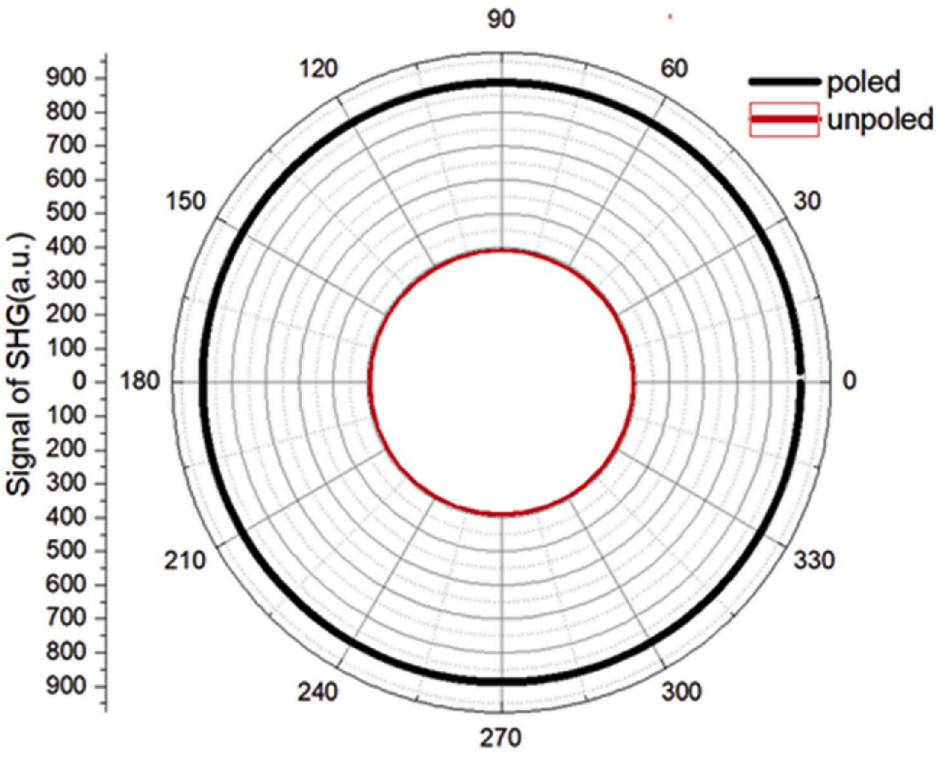

Fig. 6. Isotropic polarization pattern of SHG intensity from unpoled and poled BNT-24 ceramics, reflecting the rotation symmetry of crystal lattice.

contrast detected in the corresponding phase images (Fig. S6(b)). It also confirms the existence of irreversible field-induced phase transitions in BNT-24. Fig. S6(c) displays the phase image taken 30 min after poling, the contrast of some areas became obscure, which suggests the relaxor behaviour. The degradation of piezoelectric performance was also supported by the decreased piezoelectric coefficient (d_{33}) after poling (Table S1).

The crystal structure of BNT-24 was further investigated at nanoscale using high-resolution TEM. Bright field TEM images were taken along the [011] zone axis (Fig. 5(a)) and the [1 33] zone axis (Fig. 5(b)), respectively. It is observed that the polar structure is complex inside the grain due to the combination of domains with nanometre-sized PNRs. Furthermore, the subtle structural details were revealed by the detection of superlattice spots in the selected area electron diffraction (SAED) patterns. In Fig. 5(c), the SAED patterns along [011] zone axis exhibit $\frac{1}{2}\{ooo\}$ (*o* stands for odd Miller indices and *e* stands for even Miller indices, respectively) superlattice spots, which evidence the rhombohedral distortions. Meanwhile, the $\frac{1}{2}\{ooe\}$superlattice spots along the [1 33] zone axis are corresponding to the tetragonal distortions in Fig. 5(d). The SAED results are consistent with what is confirmed in the XRD investigation. Overall, the presence of two phases adds the complexity to the polar structure and accounts for the field-induced phase transitions, both of which are the factors contributing to a large electric field-induced strain.

To further investigate the effect of electric field on the polar structure of BNT-24, optical Second Harmonic Generation (SHG) measurements were conducted. As shown in Fig. 6, the SHG intensity is isotropic for both unpoled and poled samples, which is common for non-textured polycrystalline ceramic samples. Compared with the unpoled sample, the intensity of SHG signal is significantly enhanced after poling. Since the second-order nonlinear optical coefficient is proportional to spontaneous polarization of ferroelectrics [41], it can be inferred that the structure of BNT-24 underwent a permanent transformation at lattice scale after poling, suggesting the irreversibility of field-induced phase transitions. The result is consistent with the shape of *J-E* loops and supports the mechanism of giant strain in BNT-24.

4. Conclusion

In summary, an innovative material design was used to improve the energy conversion coefficient from the electrical energy to the mechanical energy in the BNT-based material, by enhancing the strain contributions from domain switching, field-induced phase transitions and charged point defects. An ultrahigh field-induced strain (0.74% at 70 kV/cm for unipolar) was obtained in the designed $Sr_x(Bi_{1-x}Na_{0.97-x}Li_{0.03})_{0.5}TiO_3$ (x = 0.24) sample, which is prepared via conventional solid-state reaction method. Detailed structure studies, both at global scale and local scale, attributed the giant strain to the designed short-range structural heterogeneity in BNT-24. This study not only introduced a material design strategy to achieve high-performance piezoelectric materials, but also revealed the great potential of lead-free piezoelectric materials in practical electromechanical device applications.

Declaration of competing interest

The authors declare that they have no known competing financial interests or personal relationships that could have appeared to influence the work reported in this paper.

CRediT authorship contribution statement

Jiyue Wu: Conceptualization, Methodology, Investigation, Data curation, Formal analysis, Visualization, Writing - original draft, Writing - review & editing. **Haibin Zhang:** Methodology, Data curation, Formal analysis, Visualization, Writing - review & editing. **Chang-Hsun Huang:** Data curation, Investigation, Visualization, Writing - review & editing. **Chiao-Wei Tseng:** Data curation, Writing - review & editing. **Nan Meng:** Formal analysis, Writing - review & editing. **Vladimir Koval:** Funding acquisition, Investigation, Writing - review & editing. **Yi-Chia Chou:** Funding acquisition, Supervision, Writing - review & editing. **Zhen Zhang:** Conceptualization, Funding acquisition, Supervision, Validation, Writing - review & editing. **Haixue Yan:** Conceptualization,

Methodology, Funding acquisition, Investigation, Supervision, Validation, Writing - review & editing.

Acknowledgements

Authors acknowledge the financial support by EPSRC (MASSIVE project EP/L017695/1), China Scholarship Council (CSC, 201506630005), the Grant Agency of the Slovak Academy of Sciences (VEGA Grant No. 2/0038/20), Swedish Strategic Research Foundation (to Zhen Zhang, FFL15-0174), and the Wallenberg Academy Fellow Program (to Zhen Zhang). Y. C. Chou acknowledges funding from the Ministry of Science and Technology of Taiwan under Grant No. MOST-109-2636-M-009-002, and core facility support in NCTU from MOST. This work was partially supported by the "Center for the Semiconductor Technology Research" from The Featured Areas Research Center Program within the framework of the Higher Education Sprout Project by the Ministry of Education (MOE) in Taiwan and supported in part by the Ministry of Science and Technology, Taiwan, under Grant MOST 109-2634-F-009-029.

Appendix A. Supplementary data

Supplementary data to this article can be found online at https://doi.org/10.1016/j.nanoen.2020.105037.

References

[1] H. Pan, F. Li, Y. Liu, Q. Zhang, M. Wang, S. Lan, Y. Zheng, J. Ma, L. Gu, Y. Shen, P. Yu, S. Zhang, L.-Q. Chen, Y.-H. Lin, C.-W. Nan, Ultrahigh–energy density lead-free dielectric films via polymorphic nanodomain design, Science 365 (6453) (2019) 578.

[2] D. Tan, M. Willatzen, Z.L. Wang, Prediction of strong piezoelectricity in 3R-MoS2 multilayer structures, Nano energy 56 (2019) 512–515.

[3] Z. Kutnjak, J. Petzelt, R. Blinc, The giant electromechanical response in ferroelectric relaxors as a critical phenomenon, Nature 441 (2006) 956.

[4] Y. Saito, H. Takao, T. Tani, T. Nonoyama, K. Takatori, T. Homma, T. Nagaya, M. Nakamura, Lead-free piezoceramics, Nature 432 (7013) (2004) 84.

[5] H. Jaffe, D. Berlincourt, Piezoelectric transducer materials, Proc. IEEE 53 (10) (1965) 1372–1386.

[6] L. Su, H.Y. Li, Y. Wang, S.Y. Kuang, Z.L. Wang, G. Zhu, Coupling of photoelectric and triboelectric effects as an effective approach for PZT-based high-performance self-powered ultraviolet photodetector, Nano Energy 31 (2017) 264–269.

[7] S. Zhang, F. Li, X. Jiang, J. Kim, J. Luo, X. Geng, Advantages and challenges of relaxor-PbTiO 3 ferroelectric crystals for electroacoustic transducers–A review, Prog. Mater. Sci. 68 (2015) 1–66.

[8] Y. Guo, M. Gu, H. Luo, Y. Liu, R.L. Withers, Composition-induced antiferroelectric phase and giant strain in lead-free $(Na_{0.5}Bi_{0.5})TiO_3$–$BaTiO_3$ ceramics, Phys. Rev. B 83 (5) (2011), 054118.

[9] M. Acosta, N. Novak, W. Jo, J. Rödel, Relationship between electromechanical properties and phase diagram in the $Ba(Zr_{0.2}Ti_{0.8})O_3$–$x(Ba_{0.7}Ca_{0.3})TiO_3$ lead-free piezoceramic, Acta Mater. 80 (2014) 48–55.

[10] W. Jo, R. Dittmer, M. Acosta, J. Zang, C. Groh, E. Sapper, K. Wang, J. Rödel, Giant electric-field-induced strains in lead-free ceramics for actuator applications–status and perspective, J. Electroceram. 29 (1) (2012) 71–93.

[11] W. Jo, J. Rödel, Electric-field-induced volume change and room temperature phase stability of $(Bi_{1/2}Na_{1/2})TiO_3$-x mol. % $BaTiO_3$ piezoceramics, Appl. Phys. Lett. 99 (4) (2011), 042901.

[12] X. Liu, X. Tan, Giant strains in non-textured $(Bi_{1/2}Na_{1/2})TiO_3$-based lead-free ceramics, Adv. Mater. 28 (3) (2016) 574–578.

[13] B. Narayan, J.S. Malhotra, R. Pandey, K. Yaddanapudi, P. Nukala, B. Dkhil, A. Senyshyn, R. Ranjan, Electrostrain in excess of 1% in polycrystalline piezoelectrics, Nat. Mater. 17 (5) (2018) 427–431.

[14] P. Li, J. Zhai, B. Shen, S. Zhang, X. Li, F. Zhu, X. Zhang, Ultrahigh piezoelectric properties in textured (K,Na)NbO_3-based lead-free ceramics, Adv. Mater. 30 (8) (2018), 1705171.

[15] N. Meng, X. Ren, G. Santagiuliana, L. Ventura, H. Zhang, J. Wu, H. Yan, M.J. Reece, E. Bilotti, Ultrahigh β-phase content poly(vinylidene fluoride) with relaxor-like ferroelectricity for high energy density capacitors, Nat. Commun. 10 (1) (2019) 4535.

[16] A.R. Paterson, H. Nagata, X. Tan, J.E. Daniels, M. Hinterstein, R. Ranjan, P. B. Groszewicz, W. Jo, J.L. Jones, Relaxor-ferroelectric transitions: sodium bismuth titanate derivatives, MRS Bull. 43 (8) (2018) 600–606.

[17] S.-T. Zhang, A.B. Kounga, E. Aulbach, H. Ehrenberg, J. Rödel, Giant strain in lead-free piezoceramics $Bi_{0.5}Na_{0.5}TiO_3$–$BaTiO_3$–$K_{0.5}Na_{0.5}NbO_3$ system, Appl. Phys. Lett. 91 (11) (2007), 112906.

[18] F. Li, S. Zhang, T. Yang, Z. Xu, N. Zhang, G. Liu, J. Wang, J. Wang, Z. Cheng, Z.-G. Ye, The origin of ultrahigh piezoelectricity in relaxor-ferroelectric solid solution crystals, Nat. Commun. 7 (2016) 13807.

[19] H. Nagata, T. Shinya, Y. Hiruma, T. Takenaka, I. Sakaguchi, H. Haneda, Piezoelectric properties of bismuth sodium titanate ceramics, Dev. Dielectri. Mater. Electro. Devices 167 (2012) 213–221.

[20] W. Krauss, D. Schütz, F.A. Mautner, A. Feteira, K. Reichmann, Piezoelectric properties and phase transition temperatures of the solid solution of $(1-x)(Bi_{0.5}Na_{0.5})TiO_3$–$xSrTiO_3$, J. Eur. Ceram. Soc. 30 (8) (2010) 1827–1832.

[21] V.-Q. Nguyen, H.-S. Han, K.-J. Kim, D.-D. Dang, K.-K. Ahn, J.-S. Lee, Strain enhancement in $Bi_{1/2}(Na_{0.82}K_{0.18})_{1/2}TiO_3$ lead-free electromechanical ceramics by co-doping with Li and Ta, J. Alloys Compd. 511 (1) (2012) 237–241.

[22] B.N. Rao, R. Datta, S.S. Chandrashekaran, D.K. Mishra, V. Sathe, A. Senyshyn, R. Ranjan, Local structural disorder and its influence on the average global structure and polar properties in $Na_{0.5}Bi_{0.5}TiO_3$, Phys. Rev. B 88 (22) (2013), 224103.

[23] D. Schütz, M. Deluca, W. Krauss, A. Feteira, T. Jackson, K. Reichmann, Lone-pair-induced covalency as the cause of temperature-and field-induced instabilities in bismuth sodium titanate, Adv. Funct. Mater. 22 (11) (2012) 2285–2294.

[24] B. Parija, S.K. Rout, L.S. Cavalcante, A.Z. Simões, S. Panigrahi, E. Longo, N. C. Batista, Structure, microstructure and dielectric properties of $100-x(Bi_{0.5}Na_{0.5})TiO_3-x[SrTiO_3]$ composites ceramics, Appl. Phys. A 109 (3) (2012) 715–723.

[25] C. Pascual-Gonzalez, G. Schileo, A. Khesro, I. Sterianou, D. Wang, I.M. Reaney, A. Feteira, Band gap evolution and a piezoelectric-to-electrostrictive crossover in (1 - x)$KNbO_3$-$x(Ba_{0.5}Bi_{0.5})(Nb_{0.5}Zn_{0.5})O_3$ ceramics, J. Mater. Chem. C 5 (8) (2017) 1990–1996.

[26] X. Liu, J. Zhai, B. Shen, Local phenomena in bismuth sodium titanate perovskite studied by Raman spectroscopy, J. Am. Ceram. Soc. 101 (12) (2018) 5604–5614.

[27] W. Jo, J. Daniels, D. Damjanovic, W. Kleemann, J. Rödel, Two-stage processes of electrically induced-ferroelectric to relaxor transition in $0.94(Bi_{1/2}Na_{1/2})TiO_3$-$0.06BaTiO_3$, Appl. Phys. Lett. 102 (19) (2013), 192903.

[28] C. Ma, X. Tan, E. Dul'kin, M. Roth, Domain structure-dielectric property relationship in lead-free $(1-x)(Bi_{1/2}Na_{1/2})TiO_3$-$xBaTiO_3$ ceramics, J. Appl. Phys. 108 (10) (2010), 104105.

[29] J. Suchanicz, K. Roleder, A. Kania, J. Hańaderek, Electrostrictive strain and pyroeffect in the region of phase coexistence in $Na_{0.5}Bi_{0.5}TiO_3$, Ferroelectrics 77 (1) (1988) 107–110.

[30] G. Viola, H. Ning, X. Wei, M. Deluca, A. Adomkevicius, J. Khaliq, M. John Reece, H. Yan, Dielectric relaxation, lattice dynamics and polarization mechanisms in $Bi_{0.5}Na_{0.5}TiO_3$-based lead-free ceramics, J. Appl. Phys. 114 (1) (2013), 014107.

[31] J. Wu, A. Mahajan, L. Riekehr, H. Zhang, B. Yang, N. Meng, Z. Zhang, H. Yan, Perovskite $Sr_x(Bi_{1-x}Na_{0.97-x}Li_{0.03})_{0.5}TiO_3$ ceramics with polar nano regions for high power energy storage, Nano Energy 50 (2018) 723–732.

[32] A. Khesro, D. Wang, F. Hussain, D.C. Sinclair, A. Feteira, I.M. Reaney, Temperature stable and fatigue resistant lead-free ceramics for actuators, Appl. Phys. Lett. 109 (14) (2016), 142907.

[33] L. Jin, F. Li, S. Zhang, Decoding the fingerprint of ferroelectric loops: comprehension of the material properties and structures, J. Am. Ceram. Soc. 97 (1) (2014) 1–27.

[34] H. Yan, F. Inam, G. Viola, H. Ning, H. Zhang, Q. Jiang, T.A.O. Zeng, Z. Gao, M. J. Reece, The contribution of electrical conductivity, dielectric permittivity and domain switching in ferroelectric hysteresis loops, J. Adv. Dielectr. 1 (1) (2011) 107–118.

[35] W. Jo, T. Granzow, E. Aulbach, J. Rödel, D. Damjanovic, Origin of the large strain response in $(K_{0.5}Na_{0.5})$NbO3-modified $(Bi_{0.5}Na_{0.5})TiO_3$–$BaTiO_3$ lead-free piezoceramics, J. Appl. Phys. 105 (9) (2009), 094102.

[36] J. Kling, X. Tan, W. Jo, H.J. Kleebe, H. Fuess, J. Rödel, In situ transmission electron microscopy of electric field-triggered reversible domain formation in Bi-based lead-free piezoceramics, J. Am. Ceram. Soc. 93 (9) (2010) 2452–2455.

[37] H. Simons, J. Daniels, W. Jo, R. Dittmer, A. Studer, M. Avdeev, J. Rödel, M. Hoffman, Electric-field-induced strain mechanisms in lead-free $94\%(Bi_{1/2}Na_{1/2})TiO_3$–$6\%BaTiO_3$, Appl. Phys. Lett. 98 (8) (2011), 082901.

[38] M. Eriksson, H. Yan, M. Nygren, M.J. Reece, Z. Shen, Low temperature consolidated lead-free ferroelectric niobate ceramics with improved electrical properties, J. Mater. Res. 25 (2) (2010) 240–247.

[39] X. Ren, Large electric-field-induced strain in ferroelectric crystals by point-defect-mediated reversible domain switching, Nat. Mater. 3 (2) (2004) 91–94.

[40] A.L. Kholkin, I.K. Bdikin, D.A. Kiselev, V.V. Shvartsman, S.H. Kim, Nanoscale characterization of polycrystalline ferroelectric materials for piezoelectric applications, J. Electroceram. 19 (1) (2007) 83–96.

[41] M. Vallade, Simultaneous measurements of the second harmonic generation and of the birefringence of KH_2PO_4 near its ferroelectric transition point, Phys. Rev. B 12 (9) (1975) 3755–3765.

[42] J. Hao, Z. Xu, R. Chu, W. Li, J. Du, G. Li, Ultrahigh strain response with fatigue-free behavior in $(Bi_{0.5}Na_{0.5})TiO_3$-based lead-free piezoelectric ceramics, J. Phys. D Appl. Phys. 48 (47) (2015), 472001.

[43] Y. Hiruma, T. Watanabe, H. Nagata, T. Takenaka, Piezoelectric properties of $(Bi_{1/2}Na_{1/2})TiO_3$-based solid solution for lead-free high-power applications, Jpn. J. Appl. Phys. 47 (9) (2008) 7659–7663.

[44] Y. Hiruma, H. Nagata, T. Takenaka, Detection of morphotropic phase boundary of $(Bi_{1/2}Na_{1/2})TiO_3$–$Ba(Al_{1/2}Sb_{1/2})O_3$ solid-solution ceramics, Appl. Phys. Lett. 95 (5) (2009), 052903.

[45] L. Shebanov, M. Kusnetsov, A. Sternberg, Electric field-induced antiferroelectric-to-ferroelectric phase transition in lead zirconate titanate stannate ceramics modified with lanthanum, J. Appl. Phys. 76 (7) (1994) 4301–4304.

[46] I. Dutta, R.N. Singh, Dynamic in situ X-ray diffraction study of antiferroelectric–ferroelectric phase transition in strontium-modified lead zirconate titanate ceramics, Integrated Ferroelectrics Int. J. 131 (1) (2011) 153–172.

[47] I. Dutta, R.N. Singh, Effect of electrical fatigue on the electromechanical behavior and microstructure of strontium modified lead zirconate titanate ceramics, Mater. Sci. Eng., B 166 (1) (2010) 50–60.
[48] X. Wang, J. Wu, D. Xiao, J. Zhu, X. Cheng, T. Zheng, B. Zhang, X. Lou, X. Wang, Giant piezoelectricity in potassium–sodium niobate lead-free ceramics, J. Am. Chem. Soc. 136 (7) (2014) 2905–2910.
[49] T. Zheng, J. Wu, D. Xiao, J. Zhu, X. Wang, X. Lou, Potassium–sodium niobate lead-free ceramics: modified strain as well as piezoelectricity, J. Mater. Chem. 3 (5) (2015) 1868–1874.
[50] H. Tao, J. Wu, Giant piezoelectric effect and high strain response in (1−x)($K_{0.45}Na_{0.55}$)($Nb_{1-y}Sb_y$)O_3 -x$Bi_{0.5}Na_{0.5}Zr_{1-z}Hf_zO_3$ lead-free ceramics, J. Eur. Ceram. Soc. 36 (7) (2016) 1605–1612.
[51] A.K. Kalyani, H. Krishnan, A. Sen, A. Senyshyn, R. Ranjan, Polarization switching and high piezoelectric response in Sn-modified $BaTiO_3$, Phys. Rev. B 91 (2) (2015), 024101.
[52] C. Zhao, H. Wang, J. Xiong, J. Wu, Composition-driven phase boundary and electrical properties in ($Ba_{0.94}Ca_{0.06}$)($Ti_{1-x}M_x$)O_3 (M = Sn, Hf, Zr) lead-free ceramics, Dalton Trans. 45 (15) (2016) 6466–6480.

Dr. Jiyue Wu is currently a postdoctral researcher at Uppsala University, Sweden. He received his B. Eng. Degree in Polymer Materials Science and Engineering from Donghua University (DHU) in 2015. He completed his Ph.D. degree in Materials Science at Queen Mary University of London (QMUL) in 2019. His research interest covers the synthesis of advanced dielectric and piezoelectric materials for energy storage, actuator applications, and the development of nanotransducers for clinical applications.

Prof. Haibin Zhang is a professor of the Institute of Nuclear Physics and Chemistry, China Academy of Engineering Physics (CAEP), and he is also the leader of the innovation research center for advanced nuclear materials at CAEP. Professor Zhang's research is focused on the understanding of basic principles that control properties and behaviors of advanced materials applied for next generation nuclear systems. He is an author/co-author of more than 160 scientific papers and 2 academic monographs. He is a member of the American Ceramic Society and the Chinese Ceramic Society, and serves as a reviewer for several international peer-reviewed journals.

Chang-Hsun Huang is currently a Ph.D. candidate in Electrophysics at Republic of China (Taiwan), National Chiao Tung University. He received his bachelor's degree in the Mechanical and Engineering from National Chiao Tung University in 2012. His research focuses on the growth, characterization and application of low-dimensional III-V material.

Dr. Chiao-Wei Tseng is currently a senior researcher at Topgiga material corp., Taiwan, in 2010. He received his Ph.D. degree in Chemistry at National Tsing Hua University, Taiwan. After that, he worked as post doctorate in the Institute of Chemistry at Academic Sinica, Taiwan. In 2017, he joined Dr. Zhang's group in the Division of Solid-State Electronics at Uppsala University. His research focuses on the organic-inorganic interfaces and interfacial engineering for optimization of electronic devices.

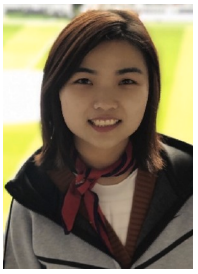

Dr. Nan Meng received her B. Eng. Degree from College of Materials Science and Engineering, Donghua University (DHU), Shanghai, China, and completed her Ph.D. in Materials Science and Engineering, Queen Mary University of London in 2017. Currently she is working as a postdoctoral fellow in the group of Dr. Emiliano Bilotti, where her research is focused on the development of polymer based dielectric capacitors for high power energy storage applications.

Dr. Vladimir Koval is a senior scientist at the Institute of Materials Research of the Slovak Academy of Sciences. He received the PhD. degree in Solid State Physics and Acoustics from Pavol Jozef Safarik University (Kosice, Slovakia) in 2001. He was awarded by the Marie-Curie Individual Fellowship (2003–2005, Queen Mary University of London, U.K.) and the Fulbright Scholarship (2006, Pennsylvania State University, U.S.A.) for outstanding research in the field of ferroelectric and piezoelectric materials. His current research interests include development of novel multiferroic materials for magnetoelectric applications and advanced dielectrics for high energy storage capacitors.

Prof. Yi-Chia Chou is an associate professor in Electrophysics at National Chiao Tung University (NCTU), Taiwan. She received her Ph.D. degree in Materials Science and Engineering from University of California Los Angeles (UCLA) in 2010. She postdoctoral research was at IBM T. J. Watson research center at Yorktown Heights, New York from 2010 to 2012, and joined NCTU in 2012. Her research interest includes materials science at nanoscale, high performance electron microscopy, and phase transformation and growth kinetics.

Prof. Zhen Zhang is a professor of solid-state electronics at Uppsala University in Uppsala, Sweden. He received the Ph.D. degree in department of microelectronics and information technology from Royal Institute of Technology (KTH) of Sweden in 2008. He worked as a research staff member at IBM T. J. Watson research center at Yorktown Heights, New York from 2008 to 2013, and joined Uppsala University in 2013. His research interest covers material science, nanoscale semiconductor devices and semiconductor based electronic sensors.

Dr. Haixue Yan is a Senior Lecturer in Materials at the School of Engineering and Materials Science in Queen Mary University of London (QMUL), where he is Deputy Chair (Education) of Division of Materials Engineering. He received his Ph.D. in Materials Science and Technology from Shanghai Institute of Ceramics, Chinese Academy of Sciences in 2001. At QMUL, his research area includes processing and analysis of the microstructures and properties of advanced materials including dielectrics, ferroelectrics, thermoelectrics, ceramic-carbon composites and metals.